Research Article
doi.org/10.1002/cplu.202100537

Chemistry Europe
European Chemical Societies Publishing

www.chempluschem.org

Ethyl Zinc β-Ketoiminates and β-Amidoenoates: Influence of Precursor Design on the Properties of Highly Conductive Zinc Oxide Thin Films from Aerosol-Assisted Chemical Vapour Deposition

Malavika A. Bhide, Claire J. Carmalt, and Caroline E. Knapp*[a]

Highly transparent (>85%) and conductive ($1.086\times10^{-3}\ \Omega$ cm) zinc oxide thin films have been deposited from specifically selected precursors allowing us to establish a direct correlation between their molecular structure and the optoelectronic properties of the deposited films. Mono-ligated ethyl zinc compounds of varying steric bulk: $[EtZn(OC(Me)CH(Me)N(^{i}Pr))]_2$ (**1**), $[EtZn(OC(OEt)CH(Me)N(^{i}Pr))]_2$ (**2**) and $[EtZn(OC(OEt)CH\text{-}H(CH_3)N(Dipp))]_2$ (**3**) were compared with the related bis-ligated zinc complexes $[Zn(OC(Me)CH(Me)N(^{i}Pr))_2]$ (**4**), $[Zn(OC(OEt)CH\text{-}(Me)N(^{i}Pr))_2]$ (**5**) and $[Zn(OC(OEt)CH(Me)N(Dipp))_2]$ (**6**). In all cases bulkier ligands resulted in poorer electronic properties of deposited films, whilst all mono-ligated compounds were shown as superior precursors. All complexes were characterised by ^{1}H and $^{13}C\{^{1}H\}$ NMR and elemental analysis, with the structure of **6** determined by single crystal X-ray diffraction. Zinc oxide films were deposited from single and dual source (with methanol) reactions of these precursors, and analysed via XRD, XPS and EDX. Optoelectronic properties were investigated through UV/vis spectroscopy and Hall effect measurements, and morphology was examined via SEM. Tauc plots from UV/vis data indicated that Film A showed the lowest band gap of 3.31 eV. Varying the elemental composition of the precursors led to changes in the elemental composition of the resultant films, as well as changes in their structural and optoelectronic properties. Using this approach of precursor design, we have been able to tune single source precursors towards zinc oxide to deposit films with specific properties.

Introduction

The deposition of zinc oxide thin films via vapour deposition techniques has a precedence in materials chemistry literature due to zinc oxide being one of the most important transparent conducting oxide (TCO) materials.[1–9] In recent years, there has been a shift towards the synthesis of single source precursors, and within this bracket, a move towards so called designer precursors, whose structural and electronic properties can be controlled at the molecular level.[10,11] A change in the structure of a molecular precursor can change the properties of the resultant film (crystallinity, phase, preferred orientation, opto-electronic properties etc.) depending on the nature of the ligands used and the geometry at the metal centre. Therefore, careful design of precursors provides the ability to fine tune their properties according to the desired application of the resultant films.

Several articles in the literature report the changes to a film depending on the temperature, substrate and solvent, but there are fewer reports of how the structure of the molecular precursor itself and the geometry around the metal centre can influence the resultant film.[12–15] The geometry index, τ quantifies the distortion at a metal centre. For four coordinate structures, $\tau_4' = 0$ and $\tau_4' = 1$ indicate a square planar geometry and a tetrahedral geometry respectively. Deviation from these values suggest that the metal centre is distorted and therefore the molecule could act as a better precursor due to its reduced stability. Zywitzki et al. reported two precursors towards nickel oxide, one with a τ_4' value of 0.81 and the other with a τ_4' value of 0.[16] The precursor with the more distorted geometry had a decomposition temperature 40 °C lower than the precursor with a non-distorted geometry, reflecting its reduced stability. Conversely, the closer the molecular geometry is to the idealised geometry in the solid state, the more favourable the deposition may be due to the similarities between the molecular and solid-state structures.[17,18] For example, alkyl zinc alkoxides have been reported as precursors towards highly textured zinc oxide films due to the facile decomposition of their cubane $[Zn\text{–}O]_4$ core, and its similarity to the bulk zinc oxide structure.[19,20] Determining which one of these scenarios is appropriate during the deposition process may help to gauge precursor merit and suitability.

There are several commercially available precursors for the deposition of zinc oxide including zinc(II) acetylacetonate, zinc alkoxides and diethyl zinc and methanol. Films produced from diethyl zinc and methanol have the lowest reported resistivities for undoped zinc oxide ($\rho = 10^{-3}$–$10^{-4}\ \Omega$ cm).[21–23] Doping zinc oxide reduces its resistivity further; aluminium-doped and

[a] M. A. Bhide, Prof. C. J. Carmalt, Dr. C. E. Knapp
Department of Chemistry
University College London
20 Gordon Street, London WC1H 0AJ (United Kingdom)
E-mail: caroline.knapp@ucl.ac.uk

Supporting information for this article is available on the WWW under https://doi.org/10.1002/cplu.202100537

gallium-doped zinc oxide films have exhibited extremely low resistivities close to the industrial standard transparent conducting oxide (TCO), namely tin-doped indium oxide (ITO) ($\Omega = 1 \times 10^{-4}$), as well as excellent optical transmission.[21,24,25] High optical transmission in TCO materials of this type can be due in part, to minimal carbon contamination. The decomposition of precursors with greater carbon content fails to compete with the facile decomposition of diethylzinc and methanol. Zinc oxide films from these precursors have greater carbon contamination which can be detrimental to optical transmission; this can render the material impractical as a TCO.[5,6,26] The one obvious advantage of these precursors is to eliminate the use of highly unstable pyrophoric reagents.

For oxide materials, oxygen content of the films can have large effects on optoelectronic properties and finding a way to control this on a molecular level is the basis of good precursor design. For single source precursors, it has been stipulated that the oxygen content in the film can be controlled by the weight % of oxygen in the precursor.[6,27] From a precursor design perspective, this relationship can be easily investigated by changing the elemental composition of the ligand and observing the effects of this on the properties of the resultant films. However, estimating oxygen content of films deposited on glass is difficult as oxygen content calculated from analytical techniques also takes into account the oxygen content of the substrate. Therefore, quantitatively estimating oxygen content of these films and making conclusions about the effect of this on the films' optoelectronic properties and relating this to the oxygen content of the precursor may neither be useful nor valid.

Here, we investigate the structural and atomic properties of zinc oxide films deposited via AACVD by systematically changing the oxygen and carbon content of the precursors used. In particular, we have chosen to use β-ketoimines and β-aminoenoates as ligands as they contain varying oxygen content, and the N donor atom offers a way to install varying degrees of carbon content into the precursors; the small ^{i}Pr (isopropyl) group and the bulky Dipp (diisopropylphenyl) groups have been used. A set of three ethyl zinc complexes and three bis-ligated zinc complexes have been synthesised and used as precursors towards zinc oxide via AACVD, and their structural and optoelectronic properties have been investigated. Some of the precursors have previously been reported and have been used in proof-of-concept studies to deposit zinc oxide but here, we conduct a detailed investigation into the influence of their molecular structure on the properties of zinc oxide thin films.

Results and Discussion

Synthesis

Ligands HL^1, HL^2 and HL^3 (Scheme 1) were synthesised from the respective 1:1 condensation reactions of the 1,3-dicarbonyl compounds acetylacetone and ethyl acetoacetate, with the primary amines isopropylamine and 2,6-diisopropylaniline. The β-ketoimine HL^1 required overnight reflux to yield the product as an orange oil whilst for the β-aminoenoates, K-10 montmorillonite clay was used as the acid catalyst allowing the reactions to proceed at room temperature. After stirring for 3 days and

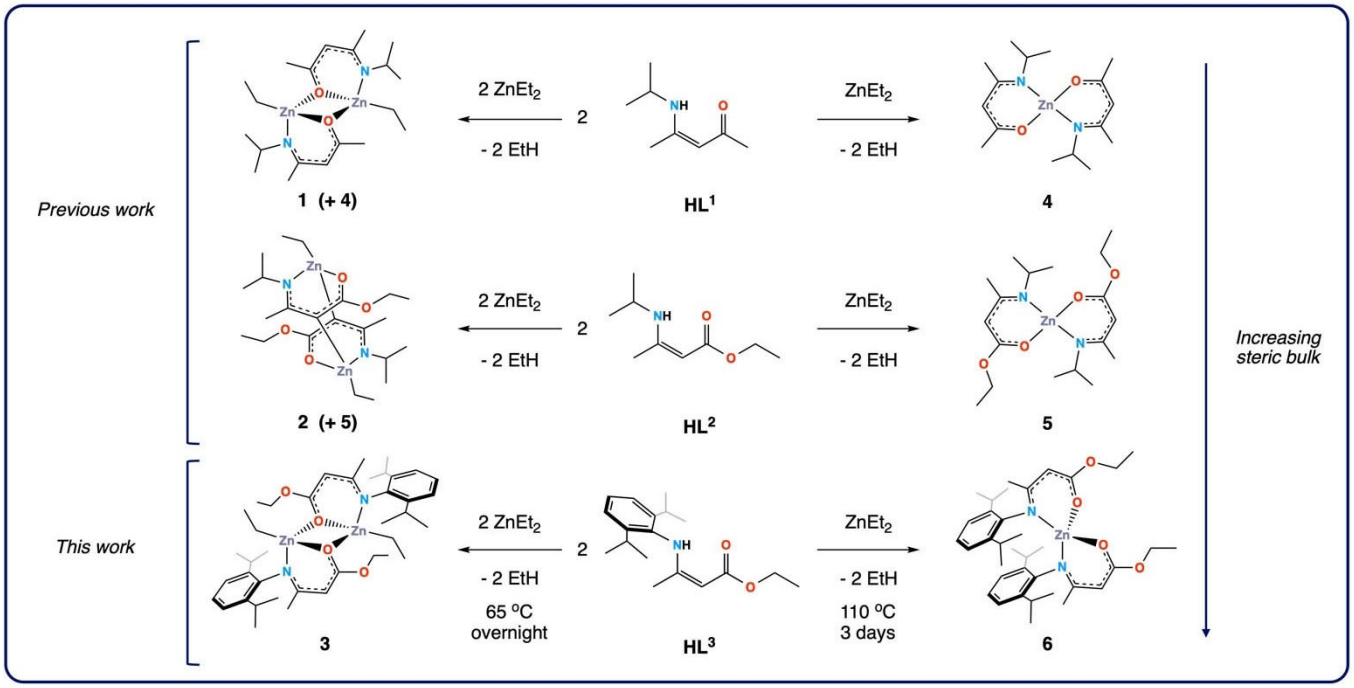

Scheme 1. Synthetic routes towards compounds **1**–**6**.

work up of the reaction mixtures, this method yielded the pale-yellow oil HL^2 and off-white solid HL^3. All three ligands were afforded in good yield and high purity as confirmed by ^1H and $^{13}C\{^1H\}$ NMR spectroscopy.

In our previous work, we showed that the reactions of diethyl zinc with HL^1 and HL^2 led to formation of the desired heteroleptic ethyl zinc compounds $[L^1ZnEt]_2$ and $[L^2ZnEt]_2$, but even when conducting the reaction at a cooled temperature with an excess of diethyl zinc, formation of the related bis-ligated complexes $[Zn(L^1)_2]$ and $[Zn(L^2)_2]$ was always observed.[28] Attempts to separate the mixtures via several methods including sublimation were unsuccessful. In this work, a ligand with a bulky R group on the N atom, namely Dipp (2,6-diisopropylphenyl), was used to investigate whether steric effects would contribute to the formation of solely the mono-ligated product. The bulky ligand was also used as a comparison of steric bulk when investigating this compound as a precursor in the CVD process.

Ethyl zinc β-ketoiminate $[L^1ZnEt]_2$ (**1**) and ethyl zinc β-amidoenoates $[L^2ZnEt]_2$ (**2**) and $[L^3ZnEt]_2$ (**3**) were synthesised from the equimolar reaction of diethylzinc with HL^1, HL^2 and HL^3 respectively in toluene (Figure 1). Unlike the reactions of HL^1 and HL^2, the reaction mixture of HL^3 and diethylzinc had to be heated to 65 °C overnight for the reaction to go to completion. The disparity in reaction conditions already demonstrates the profound effect of steric bulk on the zinc centre. Removal of the solvent yielded **3** as a viscous yellow liquid in good yield as confirmed by ^1H and $^{13}C\{^1H\}$ NMR spectroscopy.

The ^1H NMR spectrum of **3** showed sharp signals at 0.67 and 1.34 ppm in a 2:3 ratio corresponding to the protons on the bound ethyl group. The signals corresponding to the ligand protons were all shifted from the signals for free ligand protons, indicating coordination to the zinc centre. The spectrum showed no additional resonances, confirming that the bis-ligated compound $[Zn(L^3)_2]$ was not present.

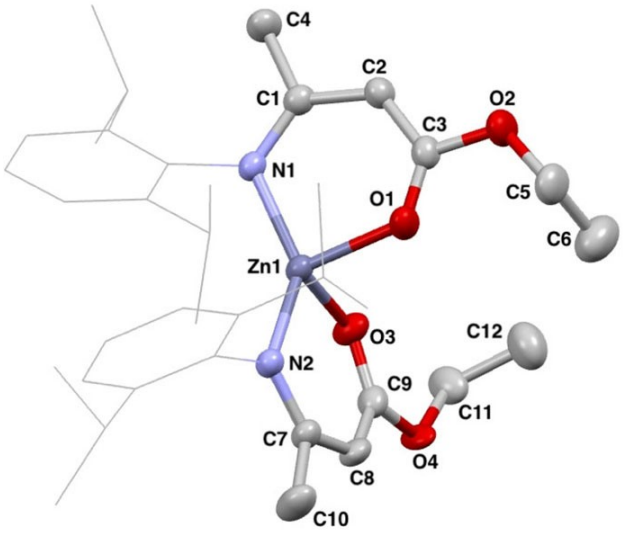

Figure 1. Solid state structure of 6 with thermal ellipsoids drawn at 50% probability and hydrogen atoms omitted for clarity.

The bis-ligated complexes $[Zn(L^1)_2]$ (**4**) and $[Zn(L^2)_2]$ (**5**) were also synthesised to compare their behaviour in the CVD process. As a further comparison, the bis-ligated complex $[Zn(L^3)_2]$ (**6**) was also synthesised and employed in CVD experiments. Compounds **4** and **5** were synthesised according to literature procedures, in a 1:2 reaction of diethylzinc with ligands HL^1 and HL^2 in toluene. The ^1H NMR spectra of **4** and **5** were concurrent with the literature.[5,24] Compound **6** was synthesised in a similar manner, however the reaction mixture needed heating to reflux for 3 days for complete conversion to the desired product. The formation of **6** was confirmed by ^1H and $^{13}C\{^1H\}$ NMR, as well as single crystal X-ray diffraction, which confirmed the structure as a monomeric species in the solid state (Figure 1).

The ^1H NMR spectrum of **6** showed two sharp signals at 1.49 and 4.86 ppm corresponding to the terminal methyl protons and methine proton of the ligand backbone respectively, as well as several broad signals corresponding to the remainder of the protons, as ascertained from COSY NMR (ESI). A similar bis-ligated aryl substituted β-diiminate (BDI) complex from the literature $[Zn(BDI\text{-}Dep)_2]$ (Dep = diethylphenyl) also shows extremely broad proton resonances.[29] Compound **6** crystallised out as a monomer in the monoclinic $P2_1/n$ space group, with the four-coordinate zinc centre adopting a highly distorted tetrahedral geometry ($\tau_4' = 0.69$). This high distortion may be due to the ligands adopting a *cis* configuration around the metal centre. We would expect the ligands to be distributed around the zinc centre in such a way as to minimise steric clashing – this is seen in complex **1**, as well as several other compounds from the literature.[5,6,30,31] The *cis* arrangement of the ligands seen in **6** may be due to C–H···π interactions between the protons on the terminal CH_3 groups and the phenyl ring on the adjacent ligand (Figure 2). The two phenyl groups are offset to facilitate this interaction, and also to alleviate steric clashing of the ^{i}Pr groups. A number of zinc aryl substituted BDI complexes from the literature exhibit similar behaviour: offset phenyl rings with protons on the adjacent phenyl substituents perpendicular to the face of ring.[29] This is also observed for a methyl substituted phenyl ring, where steric effects are lessened, further supporting the existence of a C–H···π interaction. The C–H···π distances in **6** are 2.762 Å and 2.739 Å for the two sites, which is in the range of other observed C–H···π interactions.[32]

The τ_4' values for compounds **1**–**6** were calculated and tabulated as shown in Table 1; they all exhibit some level of distortion from the ideal tetrahedral geometry. The geometry around the zinc atom in **2** and **6** is the furthest from the

Table 1. τ_4' values for compounds **1**–**6**.

Precursor	τ_4'
1	0.73
2	0.69
3	0.71
4	0.84
5	0.76
6	0.69

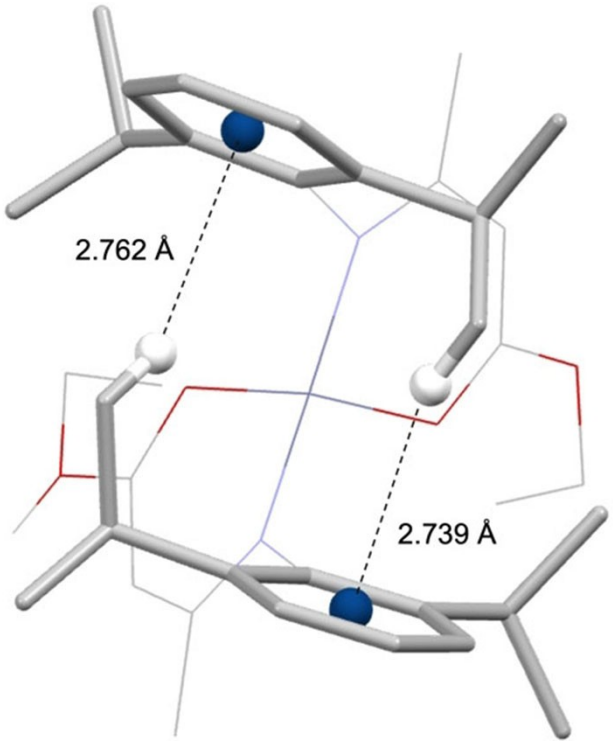

Figure 2. Structure of 6 showing C–H···π interactions.

idealised tetrahedral geometry whilst compound **4** deviates the least from this. The higher τ_4' values for **4** and **5** are as expected, due to the arrangement of two sterically unhindered bidentate ligands around the zinc centre. As mentioned above, the distortion seen in compound **6** is due to the *cis* arrangement of ligands around the zinc centre. Compounds **1**–**3** have geometries deviating from the ideal tetrahedral geometry as the monomeric unit contains a zinc atom bound to only three other atoms. The metal centre is not sterically shrouded enough to retain a monomeric structure and so dimerization occurs to achieve thermodynamic stabilisation. This dimerization involves the zinc centre having an orbital interaction with a fourth atom on an adjacent monomeric unit, arranged in such a way so as to increase orbital overlap, distorting the idealised tetrahedral geometry at the zinc centre.

AACVD

Compounds **1**–**6** were investigated as AACVD precursors towards the deposition of zinc oxide thin films. To benchmark our results, the AACVD reaction of diethylzinc with methanol was carried out, as this reaction forms zinc oxide thin films with optimal optoelectronic properties. Toluene was used as the solvent in all depositions, and methanol was used as the oxygen source in dual source reactions. A range of reaction conditions were investigated, and these are summarised in Table 2.

Single source AACVD reactions of 4, 5 and 6. Due to the reaction of HL^1 and HL^2 with diethylzinc always resulting in a mixture of the mono-ligated and bis-ligated complexes, AACVD of the bis-ligated complexes **4** and **5** was carried out to establish the influence of these complexes in the AACVD reactions of the mixtures of **1** (+**4**), and **2** (+**5**). The AACVD reaction of **6** was also carried out as a further comparison.

Table 2. Reaction conditions for the AACVD reactions of precursors **1**–**6**. Precursors were used in situ unless indicated otherwise. For depositions using precursors **1** and **2**, the numbers in parentheses are the bis-ligated species **4** and **5** that are formed during the synthesis.

Film	Single/dual source	Precursor	Temperature/[°C]
A	S	**4**	450
B	S	**5**	450
C	S	**6**	450
D	S	**1** (+**4**)	450
E	S	**2** (+**5**)	450
F	D	**1** (+**4**) (*ex situ*)	450
G	D	**2** (+**5**) (*ex situ*)	450
H	D	**3** (*ex situ*)	450
I	D	**1** (+**4**)	450
J	D	**2** (+**5**)	450
K	D	**1** (+**4**)	400
L	D	**2** (+**5**)	400
M	D	**3**	400
N	D	$ZnEt_2$	450

The single source AACVD reactions of **4**, **5** and **6** led to the deposition of non-conductive zinc oxide films **A**, **B** and **C**. X-ray diffraction patterns of the films confirmed their identity as phase pure zinc oxide, with differing levels of crystallinity (Figure 3). The XRD pattern of **A** showed a principal peak corresponding to the (101) plane, suggesting preferred orientation in this plane. Film **B** was less crystalline, showing a principal peak corresponding to the (002) plane. The XRD pattern of film **C** was not crystalline enough to assign a principal peak. The differences in the XRD patterns for these precursors already highlights the influence of their molecular arrangement. Certainly, the crystallinity of these films may also be linked to the τ_4' values of the precursors from which they were deposited; these decrease from 0.84 for **4** to 0.76 for **5** and 0.69

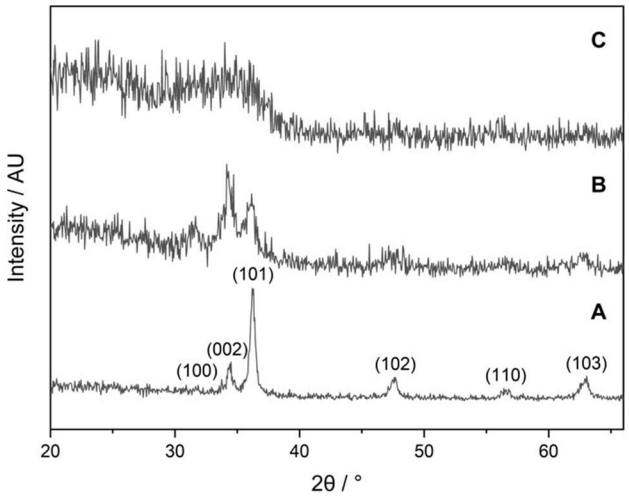

Figure 3. XRD patterns of films **A**–**C**.

for **6**. The similarity between the arrangement of the atoms in the precursor and in the bulk material may aid in the deposition process to form more crystalline films in this case.

UV/vis spectroscopy was used to ascertain the optical properties of the films. The films were brown in colour with optical light transmission of 79%, 76% and 50% at 550 nm for **A**, **B** and **C** respectively (Figure 4). Tauc plots were generated from these data to estimate the band gaps of the films (ESI); the plot for film **A** is shown in Figure 4. Film **A** had the lowest band gap of 3.31 eV, films **B** and **C** had band gaps of 3.37 eV and 3.54 eV respectively. Energy dispersive X-ray analysis (EDX) was used to confirm the presence of zinc and oxygen in the films. Carbon contamination was also quantified: film **A** had the least carbon contamination at 17.7%, with films **B** and **C** having higher percentages of carbon at 33.8 and 37.8%, as expected with increasing steric bulk. The decomposition of metal 1,3-dicarbonyl compounds is thought to be through a well-known mechanism via initial removal of the terminal alkyl β-hydrogen on the ligand backbone.[33] Amidoenoate complexes have only one site for this reaction to take place as the other side of the ligand backbone has an –OEt group attached. Therefore, we hypothesise that the decomposition of β-amidoenoate complexes may not be as facile as for β-ketoiminate complexes, resulting in more carbon contamination in films deposited from these precursors. The high carbon contamination in film **C** can also be explained by examining the TGA profile of precursor **6** which shows a final residual mass of ~25%, much higher than that expected for ZnO (~14%), due to the high level of carbon content in the precursor (ESI).

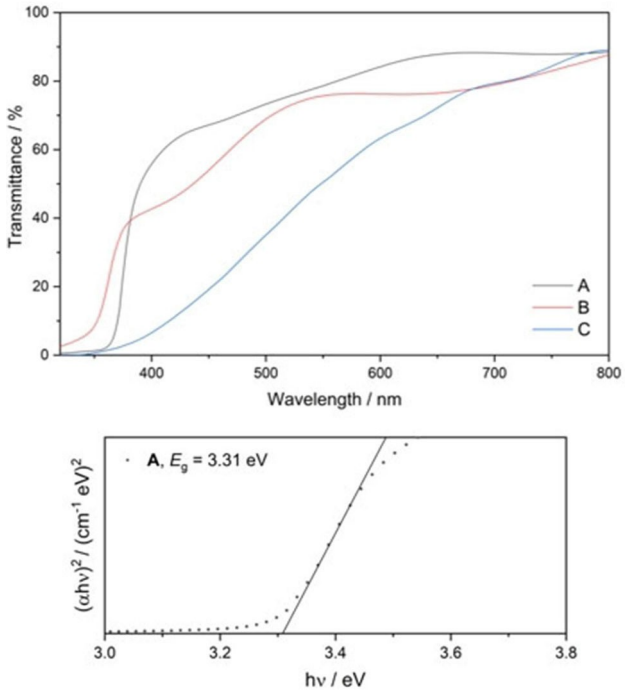

Figure 4. UV/vis transmittance spectra of films **A**–**C** (top) and representative Tauc plot of film A, showing an optical band gap of 3.31 eV (bottom).

Single source AACVD reactions of 1 and 2. After ascertaining the properties of films **A**, **B** and **C**, attention was turned to the AACVD reactions of the heteroleptic ethyl zinc complexes **1** and **2**. Although these precursors were designed to be used in dual source reactions, we initially investigated their use as single source precursors to observe their behaviour without a co-reagent, and to investigate the extent of carbon contamination.

The single source reactions of the mixtures of **1** (+**4**), and **2** (+**5**) led to the deposition of phase pure zinc oxide films, as confirmed by XRD, XPS and EDX (ESI). The XRD pattern of film **D** was very similar to that of **A**, suggesting facile decomposition of the mono-ligated precursor **1**. As compared with **B**, peaks in the XRD pattern of **E** were much broader, indicating a lesser degree of crystallinity (Figure 5).

EDX indicated greater carbon contamination in film **E** (26.7%) as compared with film **D** (11.9%), a similar trend to the films deposited from the related bis-ligated complexes (**4**–**6**). Again, the β-amidoenoate complex seems to have a less facile decomposition than the β-ketoiminate complex. The τ_4' value for **1** ($\tau_4' = 0.73$) is slightly higher than that for **2** ($\tau_4' = 0.69$) which could also justify the disparity in crystallinity of the films **D** and **E**. However, the lack of crystallinity of film **E** is most likely due to the nature of the ligand used. Even though these precursors have a direct metal-carbon bond, there is less carbon contamination than for the bis-ligated complexes, suggesting that ligand bulk plays a greater role in the levels of carbon contamination than the presence of metal-carbon bonds. The films were brown in colour with optical light transmission of 70% and 81% at 550 nm and band gaps of 3.27 and 3.29 eV for films **D** and **E** respectively. The films were extremely resistive and therefore electronic data could not be acquired. Due to the high resistivity of **D** and **E**, single source reactions with **3** were not carried out as it was predicted that they would result in the deposition of non-conductive films.

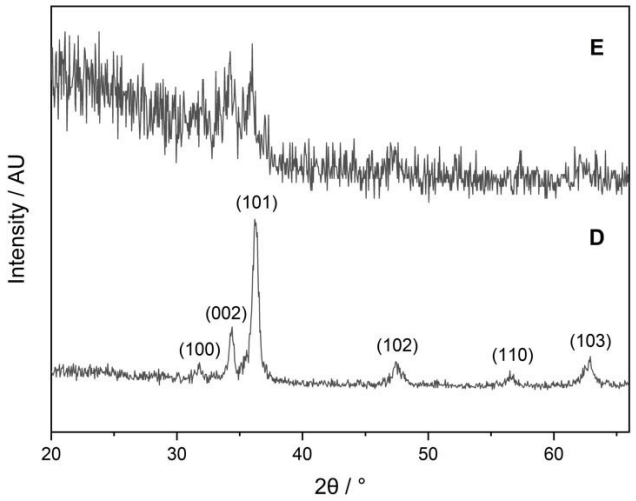

Figure 5. XRD patterns of films **D** and **E**.

Dual source AACVD reactions of 1, 2 and 3

The dual source reactions of the ethyl zinc complexes were then carried out using methanol as the oxygen source. The precursors were used as isolated solids (leading to films **F**, **G** and **H**) and *in situ* (leading to films **I** and **J**). As complex **3** was not a mixture of mono-ligated and bis-ligated complexes, the *in situ* AACVD was not carried out. Films **F**–**J** were transparent pure phase zinc oxide thin films as confirmed by XRD, XPS and EDX. They showed good coverage across the substrate and were well adhered. Though all films were confirmed as zinc oxide, XRD patterns varied according to use of isolated and *in situ* precursors (Figure 6).

Representative spectra of the Zn $2p_{3/2}$, Zn $2p_{1/2}$ and O 1s states at the surface and at a 300 s etch are shown in Figure 7. The Zn $2p_{3/2}$ and Zn $2p_{1/2}$ states appeared at 1020.7 eV and 1043.8 eV respectively and are in the range expected for zinc oxide. The O 1s peak could be deconvoluted into two separate states (i) and (ii) as shown in Figure 5. The first state (i) is attributed to the O^{2-} ions in zinc oxide. The second state (ii) can be attributed to O^{2-} vacancies in oxygen deficient areas, and also to surface bound oxygen species.[34] As the surface is etched, the second peak (ii) drastically reduces due to the reduction of surface bound oxygen species. This is also confirmed by the reduction of the atomic ratio of O/Zn in the bulk as compared to the surface (ESI).

Comparing the patterns of films **A** and **F**, there was a decrease in the intensity of the peak corresponding to the (100) plane and growth of the peak corresponding to the (002) plane, indicating that these features arise from the use of heteroleptic ethyl zinc complex **1**. Even though films **B** and **G** have the same principal peak corresponding to the (002) plane, the crystallinity of film **G** was markedly improved from that of film **B**, indicating the influence of complex **2** in the growth of **B**.

The (002) plane of zinc oxide is the most energetically stable plane as the apexes of the Zn–O tetrahedra are aligned parallel to the *c*-axis. The films using isolated precursors, **F** and **G**, gave rise to (002) plane preferential films as seen from their XRD patterns (Figure 5). For these films, there was also minimal growth in the (100) direction. XRD patterns of films **I** and **J** from *in situ* precursors had preferred orientation in the (101) plane, with minimal growth in the (002) plane. The XRD patterns of films **I**, **J** and **N** were similar and it is hypothesised that the films from *in situ* precursors have structural properties similar to films from diethylzinc and methanol as there may be an excess of diethylzinc in the *in situ* solutions (to stop formation of the bis-ligated species **4** and **5**). However, the patterns are not identical, indicating some influence from the precursors **1** and **2**. It has been suggested that oxygen rich conditions give rise to (002) preferred orientation films – in this case, the solutions using isolated precursors are more oxygen rich as there is no excess diethyl zinc. Also reported was that conditions that deteriorate tetrahedral conditions give rise to (100) and (101) preferred orientation films.[35] For the *in situ* depositions, inclusion of excess diethyl zinc may have promoted growth in the (101) plane. Film **H** had almost an equal intensity for (002) and (101) planes.

Films **F**–**J** all had excellent optical light transmission (UV/vis spectra in ESI) and their optoelectronic properties are summarised in Table 3. Film **I** had the lowest resistivity (except for film **N**) of $1.086\times10^{-3}\ \Omega$ cm. This is extremely low for undoped zinc oxide and is in the same range as film **N** and other literature value for films deposited from diethyl zinc and methanol. Film **I** exhibited a higher charge carrier concentration but a lower mobility than film **N**. The lower mobility may be due to structural defects in the films produced from carbon contamination and the less facile decomposition of the molecular precursors synthesised in this work as opposed to diethyl zinc and methanol.[1]

SEM images of films **F**, **G**, **I** and **J** are shown in Figure 8. Comparing the images of film **F** and **I**, it can be seen that the grain size of particulates in **F** is larger and more uneven than in **I**, reflecting their XRD patterns. The grain structures in films **G** and **J** are similar in shape, whilst the grain size is slightly smaller in **J**.

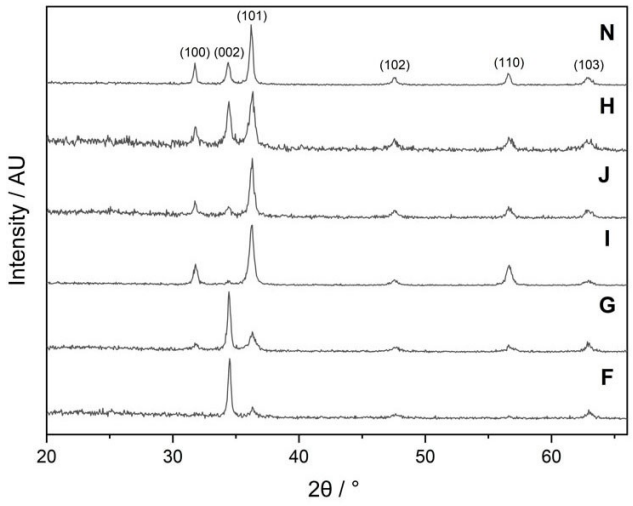

Figure 6. XRD patterns of films **F**–**J** and **N**.

Table 3. Carbon contamination, transmittance (T_λ550), band gap, resistivity (ρ), Hall mobility (μ) and charge carrier concentration (N) for films **A**–**N**.

Film	Carbon contamination/%	$T_{\lambda550}$/ %	E_g/ [eV]	ρ (10^{-3})/ [Ω cm]	μ/ [$cm^2 V^{-1} s^{-1}$]	N (10^{20})/ [cm^{-3}]
A	17.3	79	3.31	–	–	–
B	33.8	76	3.37	–	–	–
C	37.8	50	3.54	–	–	–
D	11.9	70	3.27	–	–	–
E	26.7	81	3.29	–	–	–
F	18.8	88	3.49	11.150	6.052	0.925
G	11.6	90	3.37	7.235	11.020	0.783
H	17.5	86	3.48	7.253	9.281	0.927
I	13.5	88	3.56	1.086	15.300	3.756
J	11.0	85	3.52/ 3.46	–	–	–
K	10.8	89	3.49	4.734	9.632	1.369
L	13.4	85	3.44	2.404	10.190	2.547
M	11.8	92	3.5	–	–	–
N	6.1	91	3.57	0.971	23.100	2.782

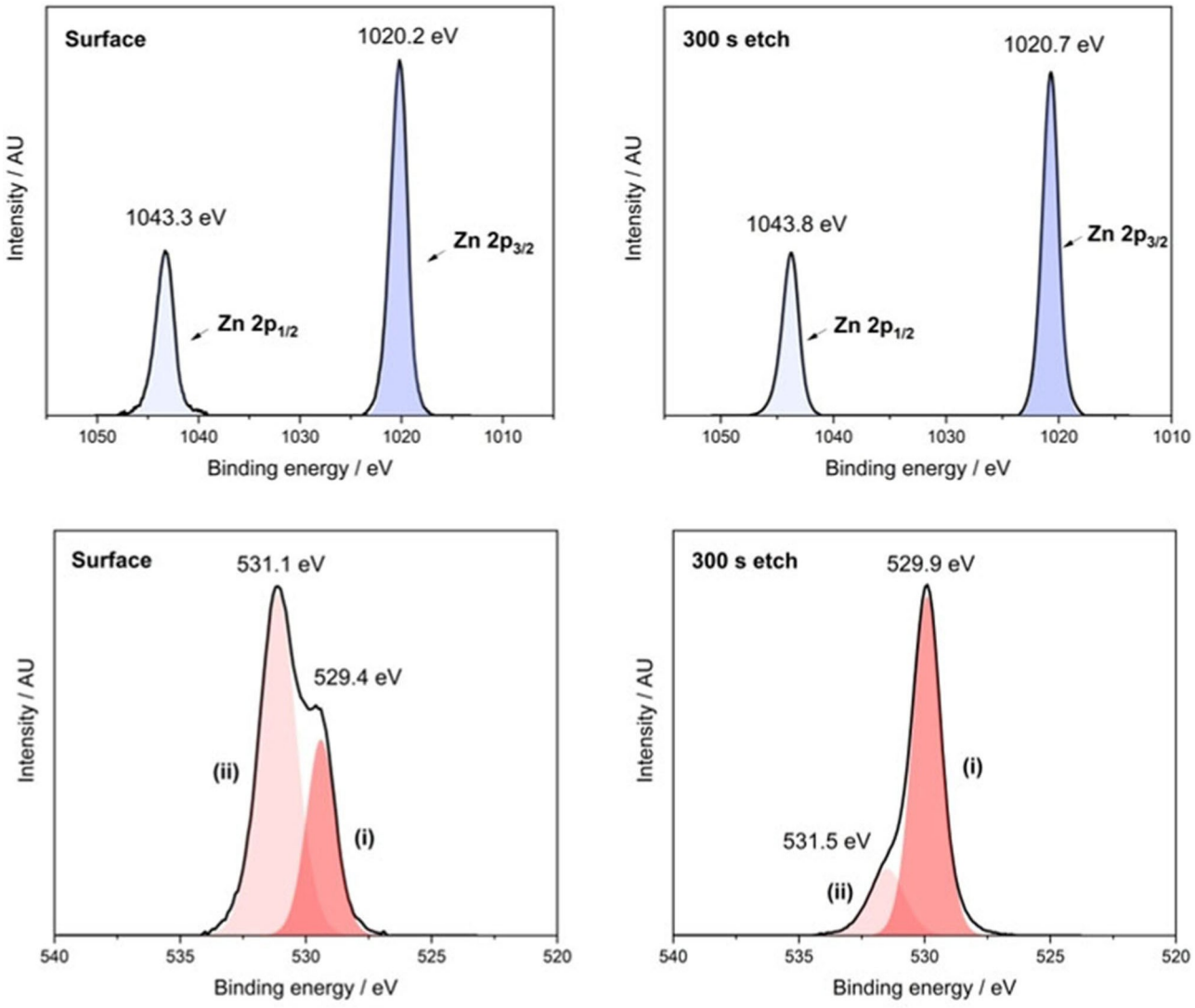

Figure 7. XPS spectra of film G showing: the Zn 2p peaks at the surface (top left), the Zn 2p peaks at a 300 s etch (top right), the O 1s peaks at the surface (bottom left) and the O 1s peaks at a 300 s etch (bottom right). (i) indicates the peak arising from the O^{2-} ions in ZnO, (ii) indicates the peak arising from O^{2-} vacancies and surface bound oxygen species.

Conclusion

This work is a comprehensive analysis of the relationship between six distinct precursors and the products of their AACVD reactions, with evidence from experimental findings showing a direct correlation between all precursors and the optoelectronic properties of the respective thin films.

From these investigations, we have shown how important the design and choice of precursor is on the properties of deposited films; this technique allows for fine tuning of precursors to achieve the desired properties for the application. Highly transparent, conductive zinc oxide films have been deposited from ethyl zinc β-ketoiminate and β-amidoenoate precursors via AACVD. The dual source AACVD reaction of ethyl zinc β-ketoiminate precursor **1** with methanol has led to the deposition of highly conductive zinc oxide thin films, with optoelectronic properties comparable to films deposited from diethyl zinc and methanol. We have shown the influence of precursor choice and design in the properties of these films, especially preferential orientation as shown from XRD. We have shown that a higher carbon content in the ligand leads to a higher percentage of carbon in the resultant films. By carrying out both single source and dual source experiments, we have shown that direct metal-carbon bonds in the precursor are less influential than the carbon content in the ligand in the incorporation of carbon in the resultant films.

Experimental Section

General procedures

All preparations were performed under an inert argon atmosphere using standard Schlenk techniques or using an MBraun nitrogen-

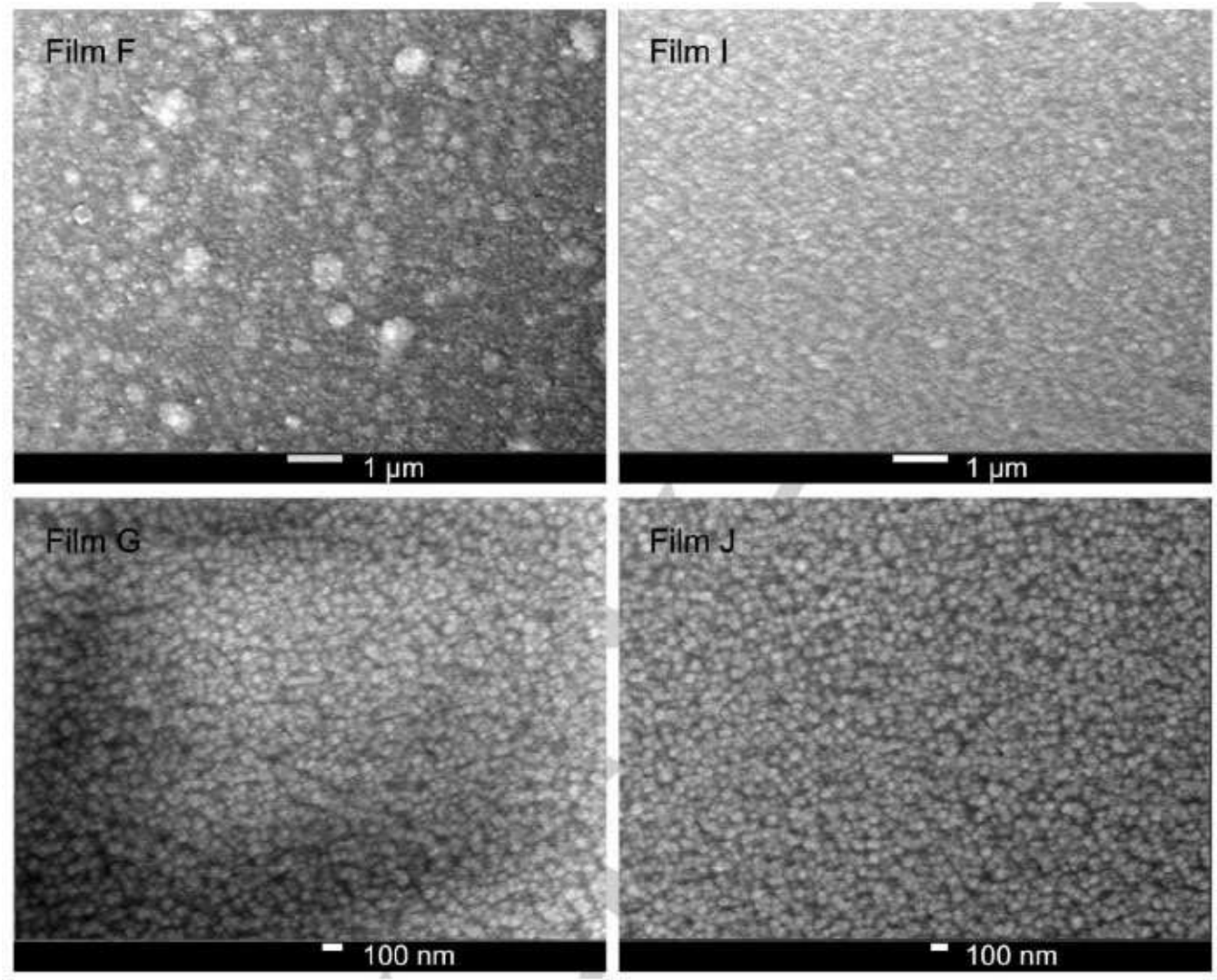

Figure 8. Top-down SEM images of films **F** and **I** both at ×11,000, film **G** at ×40,000 and film **J** at ×33,000.

filled glovebox. All chemicals were obtained from commercial sources. All solvents were obtained from a solvent purification system and stored over molecular sieves. C_6D_6 was dried using freeze-pump-thaw cycles and stored over molecular sieves. HL^1, HL^2 and HL^3, $[L^1ZnEt]_2$ (**1**), $[L^2ZnEt]_2$ (**2**), $[Zn(L^1)_2]$ (**4**) and $[Zn(L^2)_2]$ (**5**) were synthesized according to literature preparations.[5,24,28]

Single crystal X-ray diffraction (XRD) data were collected using a SuperNova Atlas (Dual) diffractometer using Cu K_α radiation of wavelength 1.54184 Å. Suitable crystals were selected and mounted on a nylon loop and the crystal was kept at 150 K during data collection. Deposition Number 2122130 (for **6**) contains the supplementary crystallographic data for this paper. These data are provided free of charge by the joint Cambridge Crystallographic Data Centre and Fachinformationszentrum Karlsruhe Access Structures service www.ccdc.cam.ac.uk/structures.T Nuclear magnetic resonance (NMR) data were recorded in C_6D_6 solutions using a Bruker Advance III 500 or 600 MHz instrument at ambient temperature unless stated otherwise. ^1H and $^{13}C\{^1H\}$ NMR assignments were confirmed by ^1H-^1H (COSY and NOESY) and ^1H-^{13}C (HSQC and HMBC) experiments where necessary. Thermogravimetric analysis (TGA) measurements were made using a PerkinElmer STA6000 TGA instrument, with a sensitivity of 0.1 mg and used N_2 as the shield gas. The samples were heated from 30 °C to 500 °C, at a heating rate of 10 °C min^{-1} under flow of shield gas.

Synthesis

Synthesis of [L^3ZnEt] (3). A solution of HL^3 (2.8912 g, 10 mmol) was added to a cooled solution of $ZnEt_2$ (1 M in hexanes) (15 cm^3, 15 mmol) in toluene (15 cm^3). The solution was brought to room temperature and stirred overnight at 65 °C. The solvent was removed to yield a viscous yellow liquid in good yield (2.98 g, 78%). ^1H NMR δ/ppm (C_6D_6, 600 MHz): 0.67 (2H, q, J = 8.1 Hz, Zn-C$\underline{H}_2$CH$_3$), 1.05 (3H, t, J = 7.1 Hz, OCH$_2$C$\underline{H}_3$), 1.08 (12H, dd, J = 6.9, 6.0 Hz, CH(C$\underline{H}_3$)$_2$), 1.34 (3H, t, J = 8.1 Hz, Zn-CH$_2$C$\underline{H}_3$), 1.46 (3H, s, NCC$\underline{H}_3$), 3.03 (2H, hept, J = 6.9 Hz, C$\underline{H}$(CH$_3$)$_2$), 4.07 (2H, q, J = 7.1 Hz, OC$\underline{H}_2$CH$_3$), 4.99 (1H, s, NCC$\underline{H}$), 6.98–7.12 (3H, aryl-$\underline{H}$). $^{13}C\{^1H\}$ NMR δ/ppm (C_6D_6, 600 MHz): −1.2 (Zn-$\underline{C}$H$_2$CH$_3$), 12.2 (Zn-CH$_2$$\underline{C}H_3$), 14.8 (OCH$_2$$\underline{C}H_3$), 23.2 (NC$\underline{C}H_3$), 24.4 (CH(C$\underline{H}_3$)$_2$), 28.3 (C$\underline{H}$(CH$_3$)$_2$), 59.9 (O$\underline{C}H_2CH_3$), 81.2 (NC$\underline{C}$H), 123.9 (aryl-$\underline{C}$), 126.4 (aryl-$\underline{C}$), 142.5 (N$\underline{C}$-(aryl)), 172.6 (N$\underline{C}$), 173.3 (O$\underline{C}$). Elemental anal. calc.%: C: 62.70, H: 8.16, N: 3.66, found%: C: 62.54, H: 8.04, N: 3.52.

Synthesis of $[Zn(L^3)_2]$ (6). A solution of HL^3 (2.8912 g, 10 mmol) was added to a cooled solution of $ZnEt_2$ (1 M in hexanes) (15 cm^3, 15 mmol) in toluene (15 cm^3). The solution was brought to room temperature and stirred to reflux for 3 days. The solvent was removed to yield a yellow solid. ^{1}H NMR δ/ppm (C_6D_6, 500 MHz): 1.05 (12H, br, $CH(C\underline{H}_3)_2$), 1.14 (6H, br, $OCH_2C\underline{H}_3$), 1.49 (6H, s, $NCC\underline{H}_3$), 2.96 (2H, br, $OC\underline{H}_2CH_3$), 3.67 (2H, br, $OC\underline{H}_2CH_3$), 4.00 (4H, br, $C\underline{H}(CH_3)_2$), 4.86 (2H, s, $NCC\underline{H}$), 7.00–7.07 (6H, m, aryl-$C\underline{H}$). $^{13}C\{^1H\}$ NMR δ/ppm (C_6D_6, 500 MHz): 14.8 ($CH(\underline{C}H_3)_2$), 23.8 ($OCH_2\underline{C}H_3$), 28.0 ($NC\underline{C}H_3$), 59.6 ($\underline{C}H(CH_3)_2$), 80.4 ($NC\underline{C}H$), 124.1 (aryl-$\underline{C}H$), 126.0 (aryl-$\underline{C}H$), 143.4 (aryl-$\underline{C}$), 144.9 ($N\underline{C}$(aryl)), 173.2 ($N\underline{C}$), 173.8 ($O\underline{C}$). Elemental anal. calc.%: C: 70.15, H: 8.31, N: 4.81, found%: C: 66.36, H: 8.07, N: 4.22.

AACVD

Depositions were carried out under argon (99.99% from BOC). Precursors (0.2 g) were dissolved in toluene (25 mL) and were placed in an AACVD glass bubbler. For deposition of film **N**, diethylzinc (1.0 M in hexanes) was placed in an AACVD bubbler with toluene (25 mL). For dual source reactions, methanol (25 mL) was placed in a second AACVD bubbler and generation of the aerosol mist was achieved using an ultrasonic humidifier containing a piezoelectric device. The aerosols were diverted through a Y-piece, transported in a flow of argon gas, through a brass baffle to a horizontal bed, cold-wall reactor fitted with a graphite block containing a Whatman cartridge heater, controlled using a Pt–Rh thermocouple. A top plate was suspended 0.5 cm above the substrate to ensure a laminar flow. The glass substrates used (15 cm × 5 cm × 0.3 cm) were cut from SiO_2, pre-coated (ca. 50 nm thick SiO_2 barrier layer) standard float glass (Pilkington NSG). Before starting depositions, the reactor and substrate were heated to the required temperature under a flow of argon gas and were left to equilibrate for ca. 10 min. After the depositions were complete, the substrate was allowed to cool to room temperature under a flow of argon gas to maintain an inert atmosphere. Films were handled and stored in air.

Physical measurements

Analysis of thin films were carried out as deposited. Grazing incident (GI)XRD patterns were recorded using a Bruker D8 Discover diffractometer. X-ray photoelectron spectroscopy (XPS) measurements were carried out on a Thermo Scientific K_α photoelectron spectrometer with a monochromatic Al K_α source. Data were calibrated against C(1s) adventitious carbon (284.6 eV) for charge correction and peaks were modelled using CasaXPS software. UV/vis transmittance spectra were produced using a Shimadzu UV-2600 spectrophotometer using an air background and recorded between 200–800 nm. Energy dispersive X-ray (EDX) analysis and scanning electron microscope (SEM) images were obtained using a JEOL JSM-7600F field emission SEM instrument on gold coated samples with an accelerating voltage of either 5 or 15 kV. Electrical properties of the films were studied by the van der Pauw method room temperature using an Ecopia HMS-3000 Hall measurement system. Square-cut samples (1 cm × 1 cm) were subjected to a 0.58 T permanent magnet and a current of 0.5 mA.

Acknowledgements

The authors would like to thank the EPSRC (EP/R513143/1) and Pilkington NSG for supplying the glass substrates. Dr Avishek Dey and Ms Shreya Mrig are thanked for carrying out XPS and TGA respectively. Dr Adam Clancy is thanked for useful scientific discussion. Mr Andrew Colton (Elemental Microanalysis Ltd.) is thanked for carrying out elemental analysis.

Conflict of Interest

The authors declare no conflict of interest.

Data Availability Statement

The data that support the findings of this study are available in the supplementary material of this article.

Keywords: optoelectronics · semiconductors · thin films · vapour deposition · zinc

[1] R. M. Pasquarelli, D. S. Ginley, R. O'Hayre, *Chem. Soc. Rev.* **2011**, *40*, 5406.
[2] S. C. Dixon, D. O. Scanlon, C. J. Carmalt, I. P. Parkin, *J. Mater. Chem. C* **2016**, *4*, 6946–6961.
[3] D. Barreca, A. P. Ferrucci, A. Gasparotto, C. Maccato, C. Maragno, E. Tondello, *Chem. Vap. Deposition* **2007**, *13*, 618–625.
[4] D. Bekermann, A. Ludwig, T. Toader, C. Maccato, D. Barreca, A. Gasparotto, C. Bock, A. D. Wieck, U. Kunze, E. Tondello, R. A. Fischer, A. Devi, *Chem. Vap. Deposition* **2011**, *17*, 155–161.
[5] J. A. Manzi, C. E. Knapp, I. P. Parkin, C. J. Carmalt, *Eur. J. Inorg. Chem.* **2015**, 3658–3665.
[6] J. S. Matthews, O. O. Onakoya, T. S. Ouattara, R. J. Butcher, *Dalton Trans.* **2006**, 3806.
[7] D. B. Potter, M. J. Powell, J. A. Darr, I. P. Parkin, C. J. Carmalt, *RSC Adv.* **2017**, *7*, 10806–10814.
[8] D. Bekermann, D. Rogalla, H. Becker, M. Winter, R. A. Fischer, A. Devi, *Eur. J. Inorg. Chem.* **2010**, 1366–1372.
[9] D. Bekermann, A. Gasparotto, D. Barreca, A. Devi, R. A. Fischer, M. Kete, U. Lavrenčič Štangar, O. I. Lebedev, C. Maccato, E. Tondello, G. Van Tendeloo, *Chem. Eur. J.* **2010**, *11*, 2337–2340.
[10] A. M. Palve, S. S. Garje, *Synth. React. Inorg. Met.-Org. Nano-Met. Chem.* **2010**, *40*, 153–156.
[11] *NANOMATERIALS VIA SINGLE-SOURCE PRECURSORS: Synthesis, Processing and Applications*, ELSEVIER, S.l., 1st edition., **2021**.
[12] D. B. Potter, I. P. Parkin, C. J. Carmalt, *RSC Adv.* **2018**, *8*, 33164–33173.
[13] G. Hyett, C. S. Blackman, I. P. Parkin, *Faraday Discuss.* **2007**, *136*, 329.
[14] N. C. Ou, X. Su, D. C. Bock, L. McElwee-White, *Coord. Chem. Rev.* **2020**, *421*, 213459.
[15] C. S. Blackman, I. P. Parkin, *Chem. Mater.* **2005**, *17*, 1583–1590.
[16] D. Zywitzki, D. H. Taffa, L. Lamkowski, M. Winter, D. Rogalla, M. Wark, A. Devi, *Inorg. Chem.* **2020**, *59*, 10059–10070.
[17] A. N. MacInnes, M. B. Power, A. R. Barron, *Chem. Mater.* **1993**, *5*, 1344–1351.
[18] S. Schulz, E. G. Gillan, J. L. Ross, L. M. Rogers, R. D. Rogers, A. R. Barron, *Organometallics* **1996**, *15*, 4880–4883.
[19] J. Auld, D. J. Houlton, A. C. Jones, S. A. Rushworth, M. A. Malik, P. O'Brien, G. W. Critchlow, *J. Mater. Chem.* **1994**, *4*, 1249.
[20] C. Sanchez-Perez, S. C. Dixon, J. A. Darr, I. P. Parkin, C. J. Carmalt, *Chem. Sci.* **2020**, *11*, 4980–4990.
[21] S. D. Ponja, S. Sathasivam, I. P. Parkin, C. J. Carmalt, *Sci. Rep.* **2020**, *10*, 638.
[22] S. D. Ponja, S. Sathasivam, I. P. Parkin, C. J. Carmalt, *RSC Adv.* **2014**, *4*, 49723–49728.
[23] D. S. Bhachu, G. Sankar, I. P. Parkin, *Chem. Mater.* **2012**, *24*, 4704–4710.
[24] C. E. Knapp, C. Dyer, N. P. Chadwick, R. Hazael, C. J. Carmalt, *Polyhedron* **2018**, *140*, 35–41.
[25] J. Nishino, S. Ohshio, K. Kamata, *J. Am. Ceram. Soc.* **1992**, *75*, 3469–3472.
[26] J. Holmes, K. Johnson, B. Zhang, H. E. Katz, J. S. Matthews, *Appl. Organomet. Chem.* **2012**, *26*, 267–272.
[27] K. L. Mears, M. A. Bhide, C. E. Knapp, C. J. Carmalt, *Dalton Trans.* **2022**, *51*, 156–167.

[28] M. A. Bhide, J. A. Manzi, C. E. Knapp, C. J. Carmalt, *Molecules* **2021**, *26*, 3165.
[29] M. Cheng, D. R. Moore, J. J. Reczek, B. M. Chamberlain, E. B. Lobkovsky, G. W. Coates, *J. Am. Chem. Soc.* **2001**, *123*, 8738–8749.
[30] I. Giebelhaus, R. Müller, W. Tyrra, I. Pantenburg, T. Fischer, S. Mathur, *Inorg. Chim. Acta* **2011**, *372*, 340–346.
[31] K. Ramasamy, M. A. Malik, M. Helliwell, J. Raftery, P. O'Brien, *Chem. Mater.* **2011**, *23*, 1471–1481.
[32] M. Nishio, Y. Umezawa, K. Honda, S. Tsuboyama, H. Suezawa, *CrystEngComm* **2009**, *11*, 1757.
[33] R. G. Gordon, S. Barry, R. N. R. Broomhall-Dillard, D. J. Teff, *Adv. Mater. Opt. Electron.* **2000**, *10*, 201–211.
[34] D. B. Potter, M. J. Powell, I. P. Parkin, C. J. Carmalt, *J. Mater. Chem. C* **2018**, *6*, 588–597.
[35] N. Fujimura, T. Nishihara, S. Goto, J. Xu, T. Ito, *J. Cryst. Growth* **1993**, *130*, 269–279.

Manuscript received: December 9, 2021
Revised manuscript received: February 26, 2022
Accepted manuscript online: March 3, 2022